



36 method, RMSE decreases by $39.95 \mu\text{g}/\text{m}^3$, and the relative deviation reduces by 44.87%.
37 Moreover, validation at two AERONET sites presents a trend closer to the true values,
38 with an R of about 0.80. This study is also a preliminary attempt to combine model-
39 driven and data-driven models, laying a foundation for further atmospheric research on
40 optimization methods.

41 **Keywords:** PM_{2.5}; Physical approach; Machine learning; Volume-to-extinction ratio;
42 Fine mode fraction

43

44 **1. Introduction**

45 Epidemiological studies have indicated that PM_{2.5} (fine particulate matter with an
46 aerodynamic equivalent diameter no greater than $2.5 \mu\text{m}$) can adversely affect human
47 health, such as increasing the risk of diabetes and respiratory diseases (Bowe et al.,
48 2018; Pope III et al., 2002; Xu et al., 2013), and accurate surface PM_{2.5} concentration
49 is the basis of air pollution-health related research. Satellite remote sensing has the
50 advantages of high resolution and global coverage (Ma et al., 2014; Wu et al., 2020),
51 including variables strongly associated with PM_{2.5} such as aerosol optical depth (AOD).
52 Therefore, it has become a mainstream method for fine particles estimation (Zhang et
53 al., 2021).

54 There are mainly three satellite-based ways of retrieving PM_{2.5}. 1) Chemical transport
55 models-based method. It calculates a scaling factor η between AOD and PM_{2.5}
56 simulated by atmospheric chemical transport models (CTM) (Lyu et al., 2022) and then
57 transfers the proportional relationship to satellite AOD data when calculating surface
58 PM_{2.5} concentration (Geng et al., 2015; Van Donkelaar et al., 2006). However, the
59 assumption of a constant factor between simulated and observed values has large
60 spatiotemporal limitations. 2) Univariate/Multivariate regression. This kind of method
61 establishes a statistical model between AOD, auxiliary variables, and ground PM_{2.5}
62 observations. Machine learning is a common tool for such data-driven methods due to
63 its powerful nonlinear fitting ability between multiple variables (Irrgang et al., 2021).
64 But the regression is affected by the distribution and density of ground stations (Gupta
65 and Christopher, 2009; Li et al., 2017). 3) Semi-empirical physical approach. Taking



66 the physical theory as the basis, surface $PM_{2.5}$ is derived through an empirical formula
67 constructed from AOD and some PM-related key parameters, including an important
68 empirical parameter related to the optical properties (S). The process steps are explicit
69 and independent of ground station observations. Meanwhile, this approach has stronger
70 physical interpretability than the previous two methods with a large space for
71 optimization.

72 Due to the complexity of the physical parameters, many studies have optimized the
73 semi-empirical physical approach. Raut and Chazette (2009) introduced a specific
74 extinction cross-section to simplify the expression of S and $PM_{2.5}$ concentration was
75 estimated based on 355nm-band radar observations. Kokhanovsky et al. (2009)
76 constructed a particle effective radius model, which can obtain the particle
77 concentrations throughout the atmospheric column. Furthermore, Zhang and Li (2015)
78 proposed the physical $PM_{2.5}$ remote sensing method (PMRS). It replaced S by defining
79 a volume-to-extinction ratio of fine particles (VE_f) and used a quadratic polynomial of
80 fine mode fraction (FMF) to simulate VE_f , showing certain advantages (Li et al., 2016;
81 Zhang et al., 2020).

82 However, the above semi-physical empirical models have some shortcomings. Firstly,
83 the satellite data used in the models are blocked by clouds and fog in some areas, thus
84 high-coverage and high-precision products need to be excavated and applied; secondly,
85 there are still large uncertainties in estimating physical parameters (such as a simple
86 polynomial fit to S in the PMRS method) and their expressions need to be improved.
87 To date, machine learning (ML) has developed rapidly. It can detect complex nonlinear
88 relationships of multiple data and model their interaction (Yuan et al., 2020; Lee et
89 al., 2022), which provides an idea for improving the accuracy of physical parameter
90 acquisition, thereby estimating high-precision $PM_{2.5}$ through semi-physical empirical
91 models.

92 According to this idea, our study proposes an optimized semi-empirical physical
93 model (RF-PMRS) based on the PMRS theory, which attempts to explore the possibility
94 of combining physical models and ML. To be specific, we creatively embed ML (the
95 random forest model) into the PMRS method to simulate the physical parameter (i.e.,



96 VE_f) derived from FMF and related variables, thus optimizing the previous polynomial
97 expression. Besides, to further improve the $PM_{2.5}$ retrieval accuracy, the physical-deep
98 learning FMF (Phy-DL FMF) dataset generated by a hybrid retrieval algorithm of ML
99 and physical mechanisms is introduced. Ultimately, we comprehensively validate the
100 performance of the $PM_{2.5}$ obtained by our optimized approach.

101 The remained part of our article is as follows. Section 2 illustrates the specific
102 derivation process of the proposed method. Section 3 describes the experimental
103 datasets and analyzes the evaluation results. Some supporting experiments are
104 discussed in section 4. And the final part provides the conclusion.

105

106 **2. Methods**

107 Based on the basic physical properties of atmospheric aerosols, the semi-physical
108 empirical approach starts from the integration of PM mass concentration and AOD.
109 Then it combines several key factors related to $PM_{2.5}$, to derive the in situ $PM_{2.5}$
110 concentration through multiple remote sensing variables (Koelemeijer et al., 2006). The
111 overall empirical relationship can be represented as:

$$112 \quad PM_{2.5} = AOD \frac{\rho}{H \cdot f(RH)} S \quad (1)$$

113 where ρ denotes the particle density and H denotes the atmospheric boundary layer
114 height. $f(RH)$ represents the hygroscopic growth factor related to relative humidity
115 (RH). S is an optical characteristic parameter that should be simulated.

116

117 **2.1. PMRS method**

118 **2.1.1. The expression of VE_f**

119 To illustrate S more precisely, PMRS defines the columnar volume-to-extinction
120 ratio of fine particles (i.e., VE_f), which can be regarded as the basis of our
121 optimization method. So equation (1) is transformed into:

$$122 \quad PM_{2.5} = AOD \frac{\rho}{H \cdot f(RH)} VE_f \quad (2)$$

123 Related to particle size, aerosol extinction, and other properties, VE_f can be



124 expressed as:

$$125 \quad VE_f = \frac{V_{f,column}}{AOD_f} \quad (3)$$

$$126 \quad AOD_f = AOD \cdot FMF \quad (4)$$

127 Here, AOD_f is the fine particle AOD and FMF is the fine mode fraction. $V_{f,column}$
 128 can be expressed by the vertical integral of particle volume size distributions (PVSD)
 129 within a certain aerodynamic diameter range:

$$130 \quad V_{f,column} = \int_0^{D_{p,c}} V(D_p) dD_p \quad (5)$$

131 $D_{p,c}$ represents the cutting diameter, and the empirical value of $2.0 \mu\text{m}$ is chosen based
 132 on previous literature (Hand and Kreidenweis, 2002; Hänel and Thudium, 1977). And
 133 $V(D_p)$ represents the PVSD corresponding to the geometric equivalent diameter (D_p).

134

135 2.1.2. Specific process and limitations

136 The PMRS method is developed from equation (2). Based on satellite AOD, the near-
 137 surface $PM_{2.5}$ can be obtained through multi-step transformation. Fig. 1(a) shows its
 138 specific process. Each arrow refers to a step, respectively: size cutting (output: AOD_f),
 139 volume visualization (output: $V_{f,column}$), bottom isolation (output: V_f , fine particle
 140 volume near the ground), particle drying (output: $V_{f,dry}$, dry V_f) and $PM_{2.5}$ weighting.

141 The overall expression is as follows:

$$142 \quad PM_{2.5} = AOD \frac{FMF \cdot VE_f \cdot \rho_{f,dry}}{PBLH \cdot f_0(RH)} \quad (6)$$

$$143 \quad f_0(RH) = \left(1 - \frac{RH}{100}\right)^{-1} \quad (7)$$

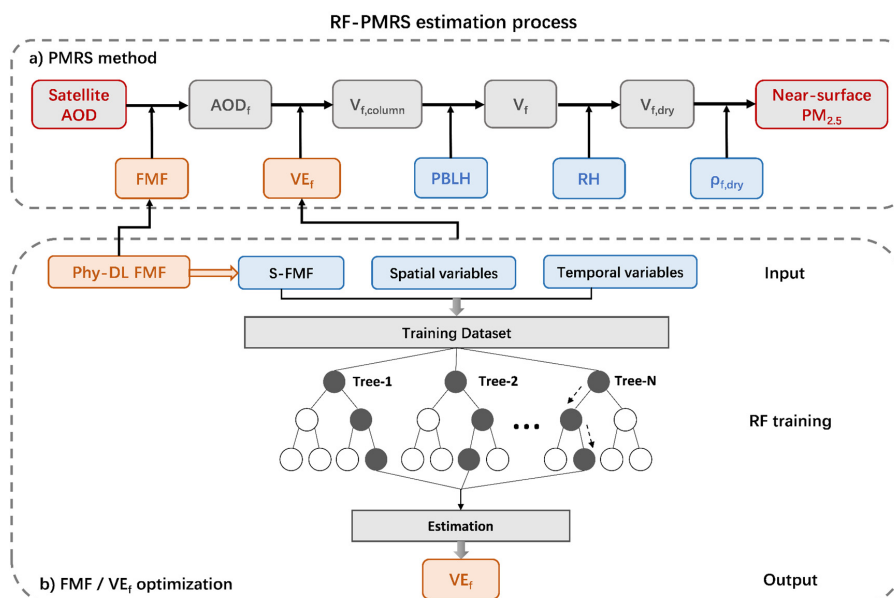
144 where FMF denotes the fine mode fraction, $\rho_{f,dry}$ denotes the dry mass density of
 145 $PM_{2.5}$, and $PBLH$ represents the planet boundary layer height. $f_0(RH)$ represents
 146 the approximation of $f(RH)$ in equation (2), as expressed as equation (7).
 147 Considering the aerosol types in different regions, PMRS fits VE_f to a quadratic
 148 polynomial relation of FMF :

$$149 \quad VE_f = 0.2887FMF^2 - 0.4663FMF + 0.356 \quad (0.1 \leq FMF \leq 1.0) \quad (8)$$



150 PMRS has strong physical significance, the calculation steps are well-defined and
 151 site-independent. Zhang and Li (2015) tested the performance of PMRS on 15 stations,
 152 and the validation results had an uncertainty of 34%. Compared with the ground value
 153 of Jinhua city in China, a 31.3% relative error was generated in Li et al. (2016). Besides,
 154 Zhang et al. (2020) applied it to the PM_{2.5} change analysis and prediction experiments
 155 in China over 20 years. However, there may be a more complex nonlinear relationship
 156 between VE_f with FMF, not just a simple quadratic formula. Since VE_f is related to the
 157 aerosol type, adding other spatiotemporal variables may optimize the fitting process.
 158 Additionally, high-quality FMF data is the basic guarantee for the estimated PM_{2.5}
 159 quality. In a word, to further improve the physical method, a better nonlinear model
 160 between VE_f and related variables from reliable datasets needs to be explored.

161



162

163 **Fig. 1.** Surface PM_{2.5} estimation flow of RF-PMRS. a) The five steps of the PMRS method. Gray
 164 boxes are the intermediate outputs, blue boxes are the input data, and orange ones denote the
 165 variables to be optimized. b) The specific optimization of RF-PMRS: FMF dataset replacement and
 166 VE_f simulation by RF model.

167

168 2.2. Optimization method: RF-PMRS

169 Therefore, to overcome the above disadvantages, an optimized method called RF-

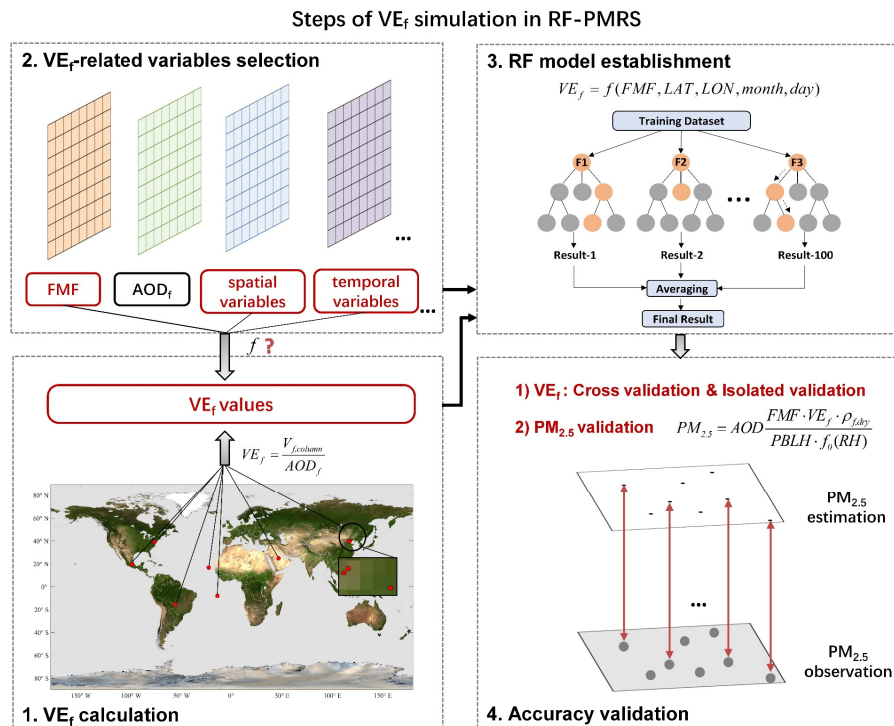


170 PMRS is proposed. Fig. 1(b) shows the process of our method, while optimizations for
 171 FMF and VE_f are described separately below.

172 **1) FMF dataset selection**

173 We introduce the Phy-DL FMF dataset into the PMRS method to improve the
 174 accuracy of size-cutting results. In the comparison experiment against Aerosol Robotic
 175 Network (AERONET) FMF, Phy-DL FMF shows a higher accuracy ($R = 0.78$, $RMSE$
 176 $= 0.100$) than Moderate-resolution Imaging Spectroradiometer (MODIS) FMF ($R =$
 177 0.37 , $RMSE = 0.282$) (Yan et al., 2022). Also, it performs better spatiotemporal
 178 continuity.

179



180
 181 **Fig. 2.** Specific steps for simulating VE_f based on ML in our RF-PMRS method. The map used in
 182 the step 1 is from NASA Visible Earth ([https://visibleearth.nasa.gov/images/57752/blue-marble-](https://visibleearth.nasa.gov/images/57752/blue-marble-land-surface-shallow-water-and-shaded-topography)
 183 [land-surface-shallow-water-and-shaded-topography](https://visibleearth.nasa.gov/images/57752/blue-marble-land-surface-shallow-water-and-shaded-topography)). The red points in step 1 represent the
 184 distribution of the 9 AERONET sites.

185

186 **2) VE_f simulation based on ML**



187 The main idea is to establish an ML model between the VE_f truth obtained from
 188 multiple AERONET sites and related variables, thus improving the subsequent VE_f -
 189 simulation accuracy (Fig. 2).

190

191 **Step 1** VE_f calculation

192 The VE_f true values are calculated concerning equations (3)-(5). A total of 9
 193 AERONET sites corresponding to four typical aerosol types participate in the training.
 194 Table 1 shows the specific information.

195

196 **Table 1.** Data information of 9 AERONET sites classified by aerosol types. Location indicates the
 197 latitude and longitude, where ‘-’ means the south latitude and west longitude. Two sites in bold fonts
 198 participate in the $PM_{2.5}$ validation experiment.

Aerosol Type	Site	Location (LAT, LON)	Training period	Isolated- validation period
	Beijing	39.98°, 116.38°	2001-2017	2018-2019
	Beijing-CAMS	39.93°, 116.32°	2012-2017	2018-2019
Urban- industrial	XiangHe	39.75°, 116.96°	2004-2017	/
	Ascension Island	-7.98°, -14.41°	2010-2017	2018-2019
	Capo Verde	16.73°, -22.94°	2010-2017	2018
Biomass burning	CUIABA	-15.73°, -56.07°	2010-2017	2018-2019
	MIRANDA			
Desert dust	GSFC	38.99°, -76.84°	2010-2017	2018-2019
	Mexico City	19.33°, -99.18°	2010-2017	/
Oceanic	Solar Village	24.91°, 46.40°	2010-2013	/

199

200 **Step 2** VE_f -related variables selection

201 According to the theory, FMF is selected as the most important modeling variable.
 202 Previous studies have also shown that the FMF- VE_f relationship has a good single-
 203 value correspondence, which is not affected by AOD. Compared with AOD_f and
 204 $V_{f,column}$, FMF is a better indicator for estimation (Zhang and Li 2015). In addition,
 205 considering the spatiotemporal heterogeneity of VE_f , the latitude, longitude (LAT,
 206 LON), and data time (month, day) of each site are added to the training.

207



208 **Step 3** RF model establishment

209 From step 2, VE_f can be expressed as:

210
$$VE_f = f(FMF, LAT, LON, month, day) \quad (9)$$

211 We optimize VE_f expression based on random forest (RF). RF is made up of multiple
212 decision trees that can build high-accuracy models based on fewer variables (Yang et
213 al., 2020). This ensemble supervised learning method randomly samples the original
214 dataset into multiple sets and considers random subsets of features in node splitting,
215 which reduces correlation and the sensitivity to noise (Belgiu and Drăguț, 2016). Note
216 that the station FMF values (S-FMF) are used when training.

217

218 **Step 4** Accuracy validation

219 The VE_f estimation is also based on equation (9), where f is the optimal relationship
220 after RF parameter adjustment, and Phy-DL FMF is applied to realize the extension of
221 model results from point to surface. 10-fold cross-validation (Rodriguez et al., 2009)
222 and isolated-validation are used to evaluate model performance (see Appendix A1).

223

224 **3) PM_{2.5} value estimation and evaluation**

225 Then, calculate PM_{2.5} according to the corresponding process (equation (6)). The
226 statistical indicators used in the evaluation include correlation coefficient (R), mean
227 bias (MB), relative mean bias (RMB), root mean square error (RMSE), and mean
228 absolute error (MAE). In addition, relative predictive error (RPE) is added to validate
229 the accuracy of the RF-based VE_f model. See Appendix A2 for the specific information
230 on these indicators.

231

232 **3. Experiment data and results**

233 **3.1. Data**

234 **3.1.1. MODIS AOD**

235 MCD19A2, the MODIS C6 Level-2 gridded (L2G) land AOD product, is selected in
236 this study. It is derived by the Multi-Angle Implementation of Atmospheric Correction



237 (MAIAC) algorithm, which can improve the accuracy in cloud detection and aerosol
238 retrieval (Lyapustin et al., 2011). Besides, this new advanced algorithm jointly
239 combines MODIS Terra and Aqua into a single sensor (Lyapustin et al., 2014). The
240 product is produced daily with a 1km resolution, including aerosol parameters such as
241 470nm/550nm AOD, quality assurance (QA), and uncertainty factors.

242 The processing of MCD19A2 data (HDF format) is mainly divided into five steps:
243 AOD/QA band extraction, best quality AOD selection, Terra/Aqua data synthesis,
244 missing information reconstruction, and mosaic. Finally, the daily AOD distribution in
245 GeoTiff format is obtained.

246

247 **3.1.2. Phy-DL FMF dataset**

248 To enhance the reliability of the global land FMF product, Yan et al. (2022) have
249 released a satellite-based dataset (daily scale) called Phy-DL FMF, which integrates
250 physical and deep learning methods. The product has a spatial resolution of 1° and
251 covers from 2001 to 2020. In terms of performance, it exhibits higher accuracy and
252 wider space-time coverage than satellite products (Yan, 2021).

253

254 **3.1.3. Meteorological data**

255 The values of PBLH and RH are obtained from the ERA5 dataset. As the fifth-
256 generation reanalysis product released by the European Center for Medium-Range
257 Weather Forecasts (ECMWF), ERA5 provides atmospheric data at 0.25° every hour
258 based on the data assimilation principle (Hersbach et al., 2018). It should be noted that
259 RH is not archived directly in ERA5, thus should be calculated by 2m temperature
260 T and dew point temperature T_d (referred to ERA-Interim: documentation).

$$261 \quad RH = 100 \times \frac{e_s(T_d)}{e_s(T)} \quad (10)$$

262 Here, $e_s(t)$ represents the saturation vapor pressure related to a Celsius temperature t
263 (Simmons et al., 1999).

$$264 \quad e_s(t) = 6.112 \times \exp\left(\frac{17.67 \times t}{t + 243.5}\right) \quad (11)$$



265

266 **3.1.4. AERONET data**

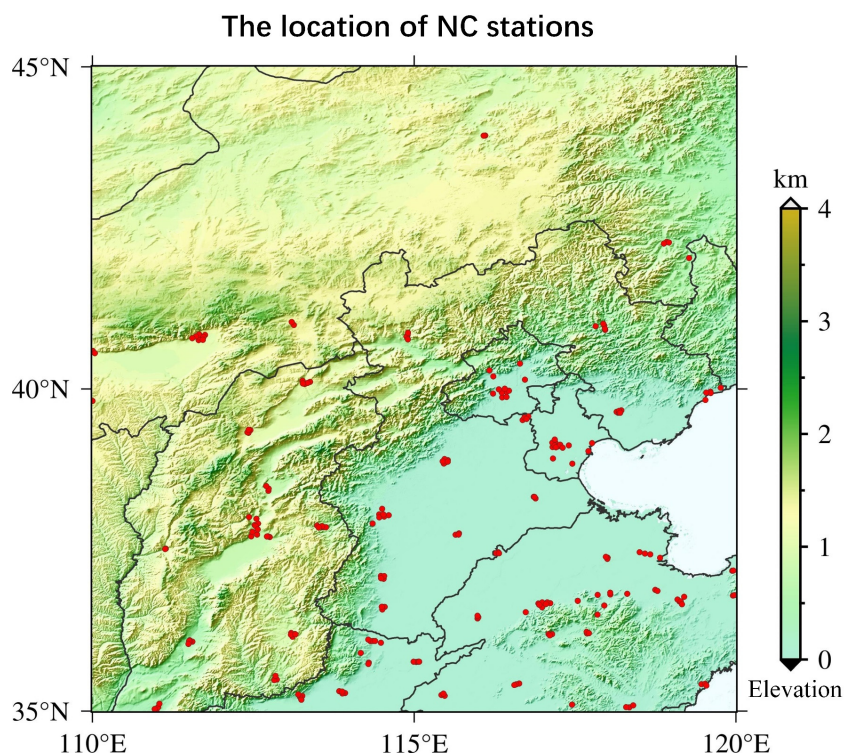
267 The Aerosol Robotic Network (AERONET) is a federation of ground-based sun-sky
268 radiometer networks, providing worldwide remote sensing aerosol data for more than
269 25 years (Holben et al., 1998). Until now, the Version 3 dataset has been released (Giles
270 et al., 2017). Due to its high quality, the data from AERONET have been regarded as
271 theoretical true values to evaluate satellite-based products in related studies (Chen et
272 al., 2020; Gao et al., 2016; Wang et al., 2019). AOD, FMF, and Volume Size
273 Distribution products with Level 2.0 (quality-assured) are applied to implement our
274 purpose.

275

276 **3.1.5. Ground PM_{2.5} measurements**

277 The near-surface hourly PM_{2.5} values are obtained from the China National
278 Environmental Monitoring Center (CNEMC). Nowadays, over 1600 ground-based
279 monitors are working continuously and a total of 232 stations (2017) in the North China
280 Region (NC) participate in this work. Fig. 3 displays the site distributions of our
281 validation area.

282



283 110°E 115°E 120°E
284 **Fig. 3.** The location of ground stations in the NC region (35°-45°N, 110°-120°E). The red points
285 represent NC stations.

286

287 The above variables are spatially matched to ground sites at their respective
288 resolutions. And based on UTC, the experiment is conducted on a daily scale in 2017.
289 Note that we select the measured empirical value of $\rho_{f,dry}$ (i.e., 1.5 g/cm³) for the NC
290 region from Gao et al. (2007).

291

292 **3.2. Experimental results**

293 **3.2.1. RF model performance for training VE_f**

294 The simulation model of VE_f is trained based on the data in Table 1 and see Appendix
295 A3 for the adjustment of the model parameters. Table 2 shows that RF can capture the
296 complex relationship between VE_f and related variables well. R is as high as 0.974
297 (0.975), RMSE and MAE are both small, and RPE is around 30%, which suggests the
298 desired estimation accuracy. Overall, the CV results represent the great performance of



299 the RF model for extracting information, that is, the relationship of multi-source data
300 to VE_f . In the meantime, the statistical results in CV and IV experiments are similar,
301 indicating that the RF model has no obvious overfitting phenomenon.

302

303 **Table 2.** Performance statistics of the RF model for training VE_f . N represents the number of data,
304 and VE_f has no unit.

	R	RMSE	RPE	MAE	N
Cross-validation (CV)	0.974	0.076	32.9%	0.034	6463
Isolated-validation (IV)	0.975	0.067	29.8%	0.037	814

305

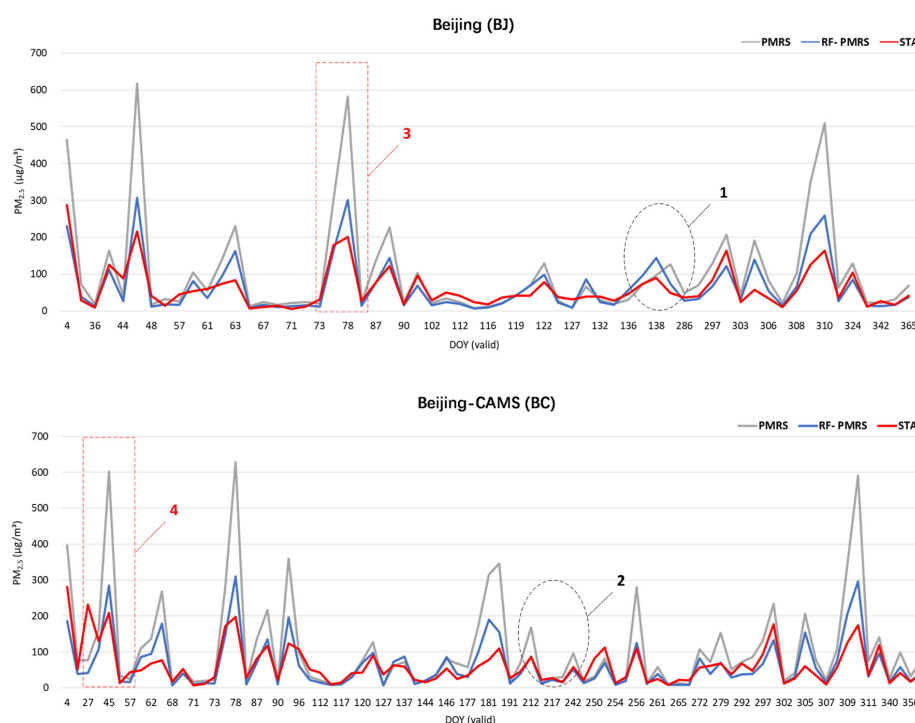
306 **3.2.2. Accuracy evaluation of PMRS/RF-PMRS at AERONET stations**

307 After applying the Phy-DL FMF data to the calculation process, the experiment
308 compares $PM_{2.5}$ results of PMRS and RF-PMRS at Beijing (BJ) and Beijing-CAMS
309 (BC) AERONET sites in 2017. Here, RF-PMRS simulates VE_f based on RF, replacing
310 the polynomial of the PMRS method. Note that the results of the two sites are compared
311 with their respective nearest ground $PM_{2.5}$ stations (distances of 3.64 km and 3.91 km,
312 respectively, in line with the representative range of ground stations in previous studies
313 (Shi et al., 2018)).

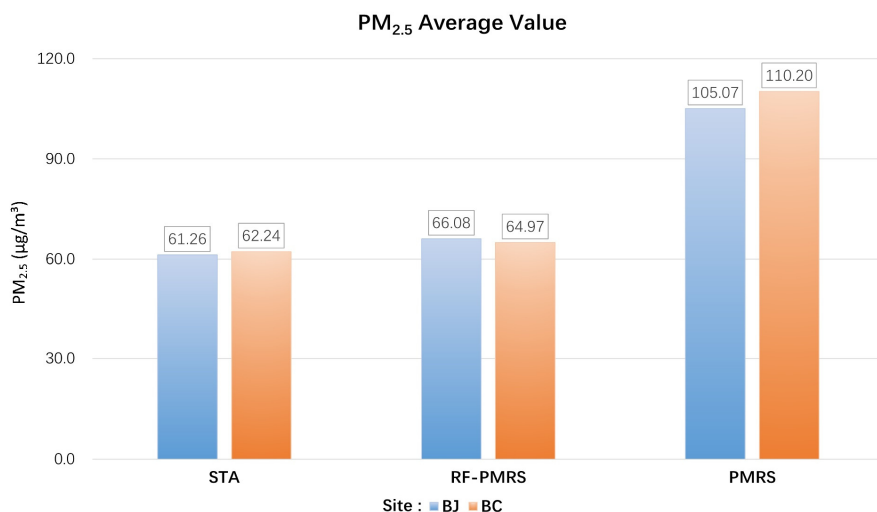
314 Fig. 4 displays the $PM_{2.5}$ value trends of different models at two sites. The blue line
315 fits the red line better than the gray one, confirming that the $PM_{2.5}$ results of RF-PMRS
316 are closer to the true values. Within the range of the black circles at positions 1 and 2,
317 the variation trend of RF-PMRS results has better consistency with the ground truth,
318 while the PMRS results show dislocation and excessive growth. The overall
319 performance of the RF-PMRS estimations can signify the effectiveness of our proposed
320 method framework. As observed in the red boxes at positions 3 and 4, both models have
321 a certain degree of deviation, which is found to be consistent with the time regularity
322 of the AOD high values. It is worth noting that our method has well mitigated the
323 apparent overestimation of the original model (PMRS) in the case of above-normal
324 aerosol loadings. Furthermore, the average $PM_{2.5}$ values from ground stations, PMRS,
325 and RF-PMRS are compared. As for the two sites, the RF-PMRS results are satisfactory.
326 As depicted in Fig. 5, the RF-PMRS and station mean values are close, with a difference



327 of $4.82 \mu\text{g}/\text{m}^3$ (BJ) and $2.73 \mu\text{g}/\text{m}^3$ (BC), suggesting a good estimation. Nevertheless,
328 the PMRS results have deviations greater than $40 \mu\text{g}/\text{m}^3$, and overestimation basically
329 exists at both sites. It can be inferred that, in our proposed method, the optimization of
330 VE_f can greatly improve the $\text{PM}_{2.5}$ estimation accuracy.
331



332
333 **Fig. 4.** Three $\text{PM}_{2.5}$ trends at the Beijing (BJ) and Beijing-CAMS (BC) sites under their respective
334 valid DOYs in 2017. Grey, blue, and red lines represent $\text{PM}_{2.5}$ values of PMRS, RF-PMRS, and
335 stations (STA), respectively. The red boxes and black circles select a specific period for analysis.
336



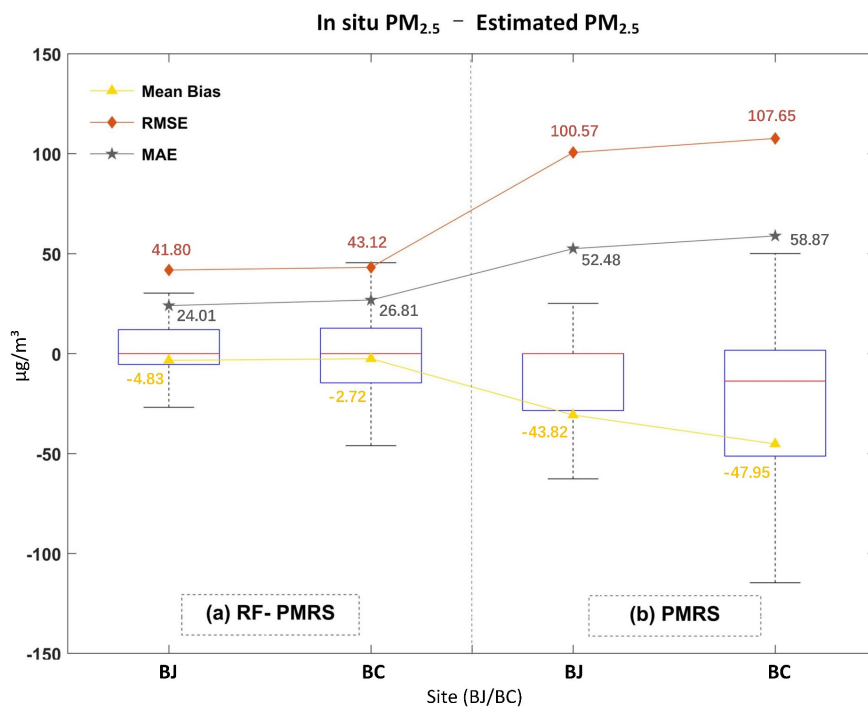
337

338 **Fig. 5.** Annual average PM_{2.5} values from stations (left), RF-PMRS (middle), and PMRS model
339 (right) at the BJ and BC sites.

340

341 Aiming at visually comparing the optimization effect, Fig. 6 plots the PM_{2.5} bias
342 distribution patterns for two methods. From the boxplot, the average PM_{2.5} bias of RF-
343 PMRS is close to zero (less than 5 µg/m³), which is greatly lower than that of PMRS.
344 Besides, PMRS PM_{2.5} has a larger deviation range, which manifests in two aspects. One
345 is the maximum bias, specifically, it has exceeded 100 µg/m³ at the BC site. The other
346 is the overall distribution of the data bias, the BJ site ones are mostly distributed below
347 zero, indicating an obvious overestimation. As for RF-PMRS, the above circumstances
348 are not obviously reflected in it. In addition, as can be seen from the indicators, RMSE
349 and MAE of RF-PMRS PM_{2.5} decrease by about half in comparison with PMRS. And
350 the experiment has confirmed that the RF-PMRS PM_{2.5} values have a strong linear
351 relationship with the ground truth at both sites, with R around 0.8 (0.82 at BJ and 0.78
352 at BC). Such a large optimization effect is attributed to the VE_f expression replacement
353 to the fitted RF model.

354



355

356 **Fig. 6.** Boxplots of RF-PMRS (a) and PMRS (b) $PM_{2.5}$ bias at the BJ and BC sites. The upper (lower)
 357 black line of each box represents the largest (smallest) value, the blue upper (lower) border
 358 represents the upper (lower) quartile, and the red line denotes the median. Besides, the yellow,
 359 orange and gray symbols are the MB, RMSE, and MAE of the corresponding $PM_{2.5}$ concentration.

360

361 3.2.3. Generalization performance of RF-PMRS

362 Then, we estimate $PM_{2.5}$ based on PMRS and RF-PMRS within North China (Fig. 3
 363 exhibits the distribution pattern of the validation stations). Table 3 shows the accuracy
 364 statistics. It can be seen that RF-PMRS greatly reduces the bias (about 44.87%), with
 365 MB of about 2.31 $\mu\text{g}/\text{m}^3$. Similar to the results at the sites, the RF-PMRS method can
 366 derive $PM_{2.5}$ concentration with practically no overestimation (underestimation).
 367 Although there is not much difference in R values of the two models (R of RF-PMRS
 368 is only improved by 0.01), RMSE and MAE of which decrease by about 39.96 $\mu\text{g}/\text{m}^3$
 369 and 18.86 $\mu\text{g}/\text{m}^3$, respectively. As a result, the optimized method deserves to be
 370 considered excellent.

371



372 **Table 3.** Validation results of PMRS and RF-PMRS $PM_{2.5}$ in North China.

Method	R	MB ($\mu\text{g}/\text{m}^3$)	RMB (%)	RMSE ($\mu\text{g}/\text{m}^3$)	MAE ($\mu\text{g}/\text{m}^3$)
PMRS	0.69	-29.34	48.71%	79.98	44.72
RF-PMRS	0.70	2.31	3.84%	40.02	25.86

373

374 Meanwhile, $PM_{2.5}$ scatterplots are presented below. As depicted in Fig. 7, there are
375 sufficient estimated samples (28305) in the NC region, which guarantees the credibility
376 of our validation results. In general, the RF-PMRS $PM_{2.5}$ values are distributed around
377 the true values evenly, with a slightly higher R of 0.70 compared to that of the original
378 method. And the slope of the linear fitting relationship reaches 0.82, which indicates
379 that the proposed method greatly reduces the overestimation of PMRS with a linear
380 slope of 1.46. Although the overall performance of the RF-PMRS estimations maintains
381 an excellent level, defects do remain. To be specific, in areas with high $PM_{2.5}$
382 concentration (especially greater than $150 \mu\text{g}/\text{m}^3$), RF-PMRS results exist a slight
383 underestimation. It may be caused by the relatively small number of high-value points
384 (only 1319 out of 28305), which is difficult to adequately reflect the fitting effect of the
385 method.

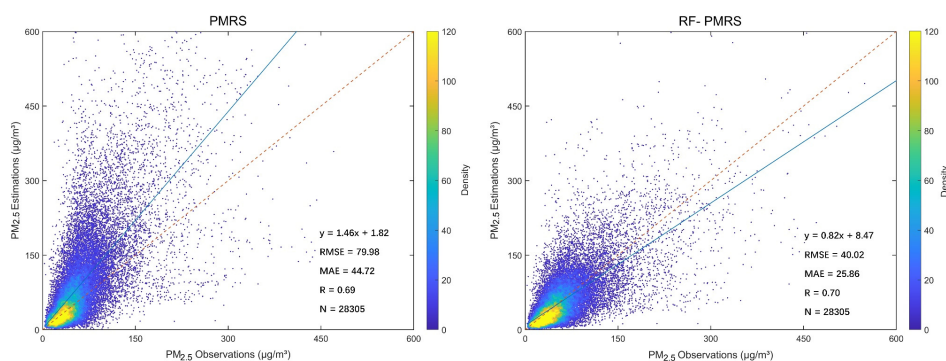
386 As for RF-PMRS, the deviation is reduced to a large extent, so the probability density
387 function maps based on the bias of PMRS and RF-PMRS are further drawn. Fig. 8
388 visualizes the probability densities within different bias ranges. In terms of distribution
389 characteristics, the overall bias of RF-PMRS from the zero value (black solid line) is
390 small. With regard to the curve shape, it is high and narrow, manifesting that the bias
391 has a lower standard deviation (STD) and is more prone to appear around the mean.
392 However, PRMS shows a more discrete distribution pattern, and there are many outliers
393 outside the range of greater than $600 \mu\text{g}/\text{m}^3$. Simultaneously, as can be concluded from
394 the three boxes, within the bias range of $\pm 20 \mu\text{g}/\text{m}^3$ and $\pm 40 \mu\text{g}/\text{m}^3$, the data numbers of
395 RF-PMRS results increase by 8.32% and 12.81%, respectively. Outside the range of
396 $\pm 100 \mu\text{g}/\text{m}^3$, the number decreases by 9.10%. Therefore, as far as the accuracy is
397 concerned, RF-PMRS results have lower bias and better stability.

398 In a word, the above analysis demonstrates that compared with the simple quadratic



399 polynomial relationship (equation (8)), the established RF model in RF-PMRS can
 400 more accurately capture the relationship between VE_f and multiple variables, thereby
 401 improving the $PM_{2.5}$ estimation accuracy.

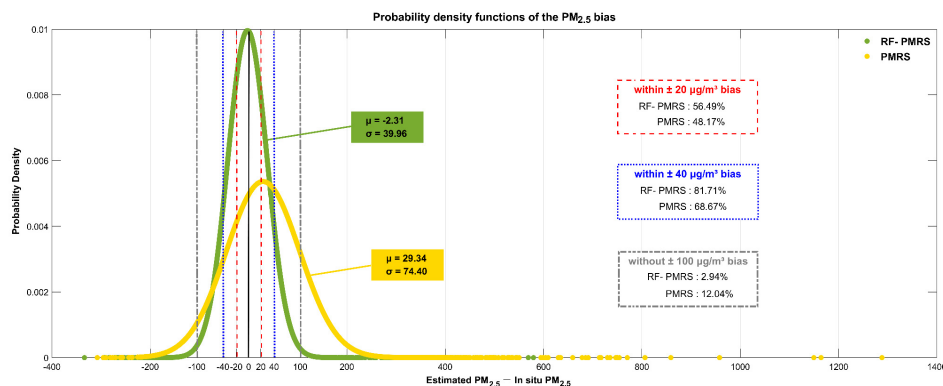
402



403

404 **Fig. 7.** Validation scatterplots of $PM_{2.5}$ results from PMRS (left) and RF-PMRS (right). Red dashed
 405 lines are 1:1 reference lines, and blue solid lines stand for the linear fits. The right legends show the
 406 point densities (frequency) represented by different colors.

407



408

409 **Fig. 8.** Probability density functions of PMRS (yellow) and RF-PMRS (green) $PM_{2.5}$ bias. The red,
 410 blue and grey dotted lines indicate the bias boundaries of $\pm 20 \mu\text{g}/\text{m}^3$, $\pm 40 \mu\text{g}/\text{m}^3$, and $\pm 100 \mu\text{g}/\text{m}^3$,
 411 respectively. μ and σ represent the mean value and standard deviation of each data.

412

413 4. Discussion

414 4.1. Accuracy comparison of PMRS using MODIS/Phy-DL FMF

415 To confirm the superiority of the Phy-FMF data adopted in our method framework,
 416 taking the BJ and BC sites as examples, the experiment compares the $PM_{2.5}$ accuracy



417 and the number of effective days calculated by PMRS based on different FMF. Table 4
418 presents the overall day-level results. As can be seen, after the FMF replacement, the
419 valid DOY turns out to become more (an increase of 113 days), which illustrates that
420 the number of effective PM_{2.5} concentration has gone up by about 5 times. Moreover,
421 the accuracy has been significantly enhanced, with R increased by about 0.30, RMSE
422 and MAE decreased by 26.14% and 16.47% accordingly. On the whole, Phy-DL FMF
423 contributes to the improvement of PMRS results, signifying the first step optimization
424 of the proposed RF-PMRS method is effective.

425

426 **Table 4.** Validation results of the PMRS method using different FMF data. The valid DOY refers to
427 the number of days that the AOD, FMF, and other data are not missing when calculating PM_{2.5}. Note
428 that since the valid days of the two schemes are different, the MB and RMB are not compared.

	Valid DOY	R	RMSE ($\mu\text{g}/\text{m}^3$)	MAE ($\mu\text{g}/\text{m}^3$)
PMRS with MODIS FMF	30	0.38	63.01	35.64
PMRS with Phy-DL FMF	143	0.68	46.54	29.77

429

430 4.2. Performance compared with other ML models

431 Different machine learning models are suitable for diverse research data, and
432 decision tree (DT) models can better fit experiments with fewer variables, such as this
433 study. For comparison, except for RF, the Extremely Randomized Tree (ERT) (Geurts
434 et al., 2006) and Gradient Boosting Decision Tree (GBDT) (Friedman, 2001) models
435 have also been established. The results of training VE_f based on the above three DT
436 models are presented in Table 5 and Table 6. By contrast, RF performs best in CV and
437 IV experiments, as indicated by the multiple accuracy indicators. Although ERT and
438 GBDT models are comparable to RF in some indicators, there exists a certain degree
439 of overfitting in the above two models, which is manifested in that their IV results are
440 clearly worse than their respective CV ones. Thus, the RF model is applied to our study.
441



442 **Table 5.** Cross-validation results in comparison of the decision tree models for training VE_f . N
443 represents the number of data, and VE_f has no unit.

CV results					
	R	RMSE	RPE	MAE	N
RF	0.974	0.076	0.330	0.034	6463
ERT	0.972	0.079	0.343	0.035	
GBDT	0.973	0.078	0.339	0.036	

444

445 **Table 6.** Isolated-validation results in comparison of the decision tree models for training VE_f . The
446 indicators are the same as those in Table 5.

IV results					
	R	RMSE	RPE	MAE	N
RF	0.975	0.067	0.299	0.037	814
ERT	0.967	0.076	0.340	0.042	
GBDT	0.969	0.074	0.331	0.040	

447

448 5. Conclusion

449 Among various satellite remote sensing methods for $PM_{2.5}$ retrieval, the semi-
450 empirical physical approach has strong physical significance and clear calculation steps,
451 and derives the $PM_{2.5}$ mass concentration independently of in situ observations.
452 However, the parameters with the meaning of optical properties are difficult to express,
453 which need to be optimized. Hence, the study proposes a method (RF-PMRS) that
454 embeds machine learning in a physical model to obtain surface $PM_{2.5}$: 1) Based on the
455 PMRS method and select the Phy-DL FMF product with a combined mechanism; 2)
456 Use the RF model to fit the parameter VE_f , rather than a simple quadratic polynomial.
457 In the point-to-surface validation, RF-PMRS shows great optimized performance.
458 Experiments at two AERONET sites show that R reaches up to 0.8. And in North China,
459 RMSE decreases by $39.95 \mu\text{g}/\text{m}^3$ with a 44.87% reduction in relative deviation. In the
460 future, we will further explore the combination of atmospheric mechanism and machine
461 learning, then research the $PM_{2.5}$ retrieval methods with physical meaning and higher
462 accuracy.

463

464 Appendix A

465 A1. 10-fold cross-validation and isolated-validation



466 The sample-based 10-fold cross-validation method is applied to test the fitting and
467 predictive ability of our model. The original dataset is randomly divided into ten parts,
468 nine of which are used as the training set for model fitting, and the remaining one is
469 used for prediction, then the cross-validation process is repeated ten rounds until each
470 data has been used as the test set.

471 At the same time, when verifying the RF-based VE_f model, the dataset in the time
472 period that did not participate in the training in Table 1 is used for isolated-validation.

473

474 **A2. Statistical indicators**

$$475 \quad R = \frac{\sum_{i=1}^m (y_i - \bar{y}) \sum_{i=1}^m (f_i - \bar{f})}{\sqrt{\sum_{i=1}^m (y_i - \bar{y})^2} \sqrt{\sum_{i=1}^m (f_i - \bar{f})^2}}$$

$$476 \quad MB = \bar{y} - \bar{f}$$

$$477 \quad RMB = \text{abs}\left(\frac{\bar{y} - \bar{f}}{\bar{y}}\right)$$

$$478 \quad RMSE = \sqrt{\frac{1}{m} \sum_{i=1}^m (y_i - f_i)^2}$$

$$479 \quad MAE = \frac{1}{m} \sum_{i=1}^m |y_i - f_i|$$

$$480 \quad RPE = \frac{\sqrt{\frac{1}{m} \sum_{i=1}^m (y_i - f_i)^2}}{\bar{y}}$$

481 where m is the total number of observations, i is the number of measurements, y_i is the
482 i -th observation, f_i is the corresponding estimation result. And \bar{y} and \bar{f} are the
483 averages of all observations and estimates, respectively.

484

485 **A3. Parameter adjustments of the RF model**

486 The four parameters of RF are adjusted, that is the correlation coefficient r changes



487 with (a) the number of trees, (b) maximum depth, (c) maximum number of features
488 when splitting, (d) minimum number of split samples. Experiments shows that the
489 maximum depth varies greatly in a small range. To prevent overfitting, the four
490 parameters of RF are adjusted to 60, 10, 2, and 8. It can ensure high accuracy while
491 improving training efficiency.

492

493 **Code and data availability**

494 All relevant codes as well as the intermediate data of this work are archived at
495 <https://doi.org/10.5281/zenodo.7183822> (Jin, 2022). The MCD19A2 data can be
496 downloaded on <https://ladsweb.modaps.eosdis.nasa.gov> (last access: 30-09-2022)
497 (Lyapustin and Wang, 2015). Detailed information about Phy-DL FMF dataset can be
498 found at <https://doi.org/10.5281/zenodo.5105617> (Yan, 2021). Meteorological data
499 used in this work are obtained on
500 <https://cds.climate.copernicus.eu/cdsapp#!/dataset/reanalysis-era5-single-levels> (last
501 access: 30-09-2022) (Hersbach et al., 2018). AERONET data was downloaded from
502 <https://aeronet.gsfc.nasa.gov/> (last access: 30-09-2022) (Giles et al., 2019).

503

504 **Author contributions**

505 **Caiyi Jin:** Data curation, Methodology, Formal analysis, Writing - original draft.
506 **Qiangqiang Yuan:** Conceptualization, Supervision, Project administration, Writing -
507 review and editing. **Tongwen Li:** Resources, Methodology, Writing - review and
508 editing, Formal analysis. **Yuan Wang:** Methodology, Validation, Writing - review and
509 editing. **Liangpei Zhang:** Supervision, Writing - review and editing.

510

511 **Competing interests**

512 The contact author has declared that none of the authors has any competing interests.

513

514 **Acknowledgments**

515 We gratefully acknowledge the Atmosphere Archive and Distribution System
516 (LAADS), the ECMWF, the AERONET project, and the CNEMC for respectively



517 providing the MODIS products, the meteorological data, the ground aerosol data, and
518 the surface PM_{2.5} concentration. We also thank other institutions which provide related
519 data in this work.

520

521 **Financial support**

522 This research was funded in part by the National Natural Science Foundation of
523 China (41922008) and the Hubei Science Foundation for Distinguished Young Scholars
524 (2020CFA051).

525

526 **References**

527 Belgiu, M., and Drăguț, L.: Random forest in remote sensing: A review of applications
528 and future directions, *ISPRS J. Photogramm. Remote Sens.*, 114, 24-31,
529 <https://doi.org/10.1016/j.isprsjprs.2016.01.011>, 2016.

530 Bowe, B., Xie, Y., Li, T., Yan, Y., Xian, H., and Al-Aly, Z.: The 2016 global and
531 national burden of diabetes mellitus attributable to PM_{2.5} air pollution, *Lancet Planet.
532 Health*, 2, e301-e312, [https://doi.org/10.1016/S2542-5196\(18\)30140-2](https://doi.org/10.1016/S2542-5196(18)30140-2), 2018.

533 Chen, X., de Leeuw, G., Arola, A., Liu, S., Liu, Y., Li, Z., and Zhang, K.: Joint retrieval
534 of the aerosol fine mode fraction and optical depth using MODIS spectral reflectance
535 over northern and eastern China: Artificial neural network method, *Remote Sens
536 Environ*, 249, 112006, <https://doi.org/10.1016/j.rse.2020.112006>, 2020.

537 Friedman, J.H.: Greedy function approximation: a gradient boosting machine, *Ann Stat*,
538 29(5), 1189–1232, <http://www.jstor.org/stable/2699986>, 2001.

539 Gao, J., Zhou, Y., Wang, J., Wang, T., and Wang, W.X.: Inter-comparison of WPSTM-
540 TEOMTM-MOUDITM and investigation on particle density, *Huan Jing Ke Xue*, 28,
541 1929-1934, <https://doi.org/10.3321/j.issn:0250-3301.2007.09.005>, 2007.

542 Gao, L., Li, J., Chen, L., Zhang, L., and Heidinger, A.K.: Retrieval and validation of
543 atmospheric aerosol optical depth from AVHRR over China, *IEEE Trans Geosci
544 Remote Sens*, 54, 6280-6291, <https://doi.org/10.1109/TGRS.2016.2574756>, 2016.

545 Geng, G., Zhang, Q., Martin, R.V., van Donkelaar, A., Huo, H., Che, H., Lin, J., and
546 He, K.: Estimating long-term PM_{2.5} concentrations in China using satellite-based



547 aerosol optical depth and a chemical transport model, *Remote Sens Environ*, 166, 262-
548 270, <https://doi.org/10.1016/j.rse.2015.05.016>, 2015.

549 Geurts, P., Ernst, D., and Wehenkel, L.: Extremely randomized trees, *Mach Learn*, 63,
550 3-42, <https://doi.org/10.1007/s10994-006-6226-1>, 2006.

551 Giles, D.M., Holben, B.N., Eck, T.F., Smirnov, A., Sinyuk, A., Schafer, J., Sorokin,
552 M.G., and Slutsker, I.: Aerosol robotic network (AERONET) version 3 aerosol optical
553 depth and inversion products, in: American Geophysical Union (AGU) 98th Fall
554 Meeting Abstracts, New Orleans, America, 11-15 December 2017, A11O-01, 2017.

555 Giles, D. M., Sinyuk, A., Sorokin, M. G., Schafer, J. S., Smirnov, A., Slutsker, I., Eck,
556 T. F., Holben, B. N., Lewis, J. R., Campbell, J. R., Welton, E. J., Korokin, S. V., and
557 Lyapustin, A. I.: Advancements in the Aerosol Robotic Network (AERONET) Version
558 3 database - automated near-real-time quality control algorithm with improved cloud
559 screening for Sun photometer aerosol optical depth (AOD) measurements, *Atmos Meas*
560 *Tech*, 12, 169–209, <https://doi.org/10.5194/amt-12-169-2019>, 2019.

561 Gupta, P., and Christopher, S.A.: Particulate matter air quality assessment using
562 integrated surface, satellite, and meteorological products: Multiple regression approach,
563 *J. Geophys. Res. Atmos.*, 114, D14205, <https://doi.org/10.1029/2008JD011496>, 2009.

564 Hand, J.L., and Kreidenweis, S.M.: A new method for retrieving particle refractive
565 index and effective density from aerosol size distribution data, *Aerosol Sci Technol*, 36,
566 1012-1026, <https://doi.org/10.1080/02786820290092276>, 2002.

567 Hänel, G., and Thudium, J.: Mean bulk densities of samples of dry atmospheric aerosol
568 particles: A summary of measured data, *Pure Appl. Geophys.*, 115, 799-803,
569 <https://doi.org/10.1007/BF00881211>, 1977.

570 Hersbach, H., Bell, B., Berrisford, P., Biavati, G., Horányi, A., Muñoz Sabater, J.,
571 Nicolas, J., Peubey, C., Radu, R., Rozum, I., Schepers, D., Simmons, A., Soci, C., Dee,
572 D., Thépaut, J-N.: ERA5 hourly data on single levels from 1979 to present, Copernicus
573 Climate Change Service (C3S) Climate Data Store (CDS) [data set], (Accessed on 30-
574 09-2022), <https://doi.org/10.24381/cds.adbb2d47>, 2018.

575 Holben, B.N., Eck, T.F., Slutsker, I., Tanré, D., Buis, J.P., Setzer, A., Vermote, E.,



576 Reagan, J.A., Kaufman, Y.J., Nakajima, T., Lavenu, F., Jankowiak, I., and Smirnov, A.:
577 AERONET — A federated instrument network and data archive for aerosol
578 characterization, *Remote Sens Environ*, 66, 1-16, [https://doi.org/10.1016/S0034-](https://doi.org/10.1016/S0034-4257(98)00031-5)
579 [4257\(98\)00031-5](https://doi.org/10.1016/S0034-4257(98)00031-5), 1998.

580 Irrgang, C., Boers, N., Sonnewald, M., Barnes, E.A., Kadow, C., Staneva, J., and
581 Saynisch-Wagner, J.: Towards neural Earth system modelling by integrating artificial
582 intelligence in Earth system science, *Nat. Mach. Intell.*, 3, 667-674,
583 <https://doi.org/10.1038/s42256-021-00374-3>, 2021.

584 Jin, C.: An optimized semi-empirical physical approach for satellite-based PM_{2.5}
585 retrieval: using random forest model to simulate the complex parameter, Zenodo [code],
586 <https://doi.org/10.5281/zenodo.7183822>, 2022.

587 Koelemeijer, R.B.A., Homan, C.D., and Matthijsen, J.: Comparison of spatial and
588 temporal variations of aerosol optical thickness and particulate matter over Europe,
589 *Atmospheric Environ.*, 40, 5304-5315, <https://doi.org/10.1016/j.atmosenv.2006.04.044>,
590 2006.

591 Kokhanovsky, A.A., Prikhach, A.S., Katsev, I.L., and Zege, E.P.: Determination of
592 particulate matter vertical columns using satellite observations, *Atmos Meas Tech*, 2,
593 327-335, <https://doi.org/10.5194/amt-2-327-2009>, 2009.

594 Lee, J.-B., Lee, J.-B., Koo, Y.-S., Kwon, H.-Y., Choi, M.-H., Park, H.-J., and Lee, D.-
595 G.: Development of a deep neural network for predicting 6 h average PM_{2.5}
596 concentrations up to 2 subsequent days using various training data, *Geosci. Model Dev.*,
597 15, 3797–3813, <https://doi.org/10.5194/gmd-15-3797-2022>, 2022.

598 Li, T., Shen, H., Zeng, C., Yuan, Q., and Zhang, L.: Point-surface fusion of station
599 measurements and satellite observations for mapping PM_{2.5} distribution in China:
600 Methods and assessment, *Atmospheric Environ.*, 152, 477-489,
601 <https://doi.org/10.1016/j.atmosenv.2017.01.004>, 2017.

602 Li, Z., Zhang, Y., Shao, J., Li, B., Hong, J., Liu, D., Li, D., Wei, P., Li, W., Li, L.,
603 Zhang, F., Guo, J., Deng, Q., Wang, B., Cui, C., Zhang, W., Wang, Z., Lv, Y., Xu, H.,
604 Chen, X., Li, L., and Qie, L.: Remote sensing of atmospheric particulate mass of dry
605 PM_{2.5} near the ground: Method validation using ground-based measurements, *Remote*



- 606 Sens Environ, 173, 59-68, <https://doi.org/10.1016/j.rse.2015.11.019>, 2016.
- 607 Lyapustin, A., Wang, Y., Laszlo, I., Kahn, R., Korkin, S., Remer, L., Levy, R., and
608 Reid, J.S.: Multiangle implementation of atmospheric correction (MAIAC): 2. Aerosol
609 algorithm, J. Geophys. Res. Atmos., 116, D03211,
610 <https://doi.org/10.1029/2010JD014986>, 2011.
- 611 Lyapustin, A., Wang, Y., Xiong, X., Meister, G., Platnick, S., Levy, R., Franz, B.,
612 Korkin, S., Hilker, T., Tucker, J., Hall, F., Sellers, P., Wu, A., and Angal, A.: Scientific
613 impact of MODIS C5 calibration degradation and C6+ improvements, Atmos Meas
614 Tech, 7, 4353-4365, <https://doi.org/10.5194/amt-7-4353-2014>, 2014.
- 615 Lyapustin, A., and Wang, Y.: MCD19A2 MODIS/Terra+Aqua Aerosol Optical
616 Thickness Daily L2G Global 1km SIN Grid, NASA LP DAAC [data set], (Accessed
617 on 30-09-2022), <http://doi.org/10.5067/MODIS/MCD19A2.006>, 2015.
- 618 Lyu, B., Huang, R., Wang, X., Wang, W., and Hu, Y.: Deep-learning spatial principles
619 from deterministic chemical transport models for chemical reanalysis: an application in
620 China for PM_{2.5}, Geosci. Model Dev., 15, 1583–1594, [https://doi.org/10.5194/gmd-](https://doi.org/10.5194/gmd-15-1583-2022)
621 [15-1583-2022](https://doi.org/10.5194/gmd-15-1583-2022), 2022.
- 622 Ma, Z., Hu, X., Huang, L., Bi, J., and Liu, Y.: Estimating ground-level PM_{2.5} in China
623 using satellite remote sensing, Environ. Sci. Technol., 48, 7436-7444,
624 <https://doi.org/10.1021/es5009399>, 2014.
- 625 Pope III, C.A., Burnett, R.T., Thun, M.J., Calle, E.E., Krewski, D., Ito, K., and Thurston,
626 G.D.: Lung cancer, cardiopulmonary mortality, and long-term exposure to fine
627 particulate air pollution, JAMA, 287, 1132-1141,
628 <https://doi.org/10.1001/jama.287.9.1132>, 2002.
- 629 Raut, J., and Chazette, P.: Assessment of vertically-resolved PM₁₀ from mobile lidar
630 observations, Atmospheric Chem. Phys., 9, 8617-8638, [https://doi.org/10.5194/acp-9-](https://doi.org/10.5194/acp-9-8617-2009)
631 [8617-2009](https://doi.org/10.5194/acp-9-8617-2009), 2009.
- 632 Rodriguez, J.D., Perez, A., and Lozano, J.A.: Sensitivity analysis of k-fold cross
633 validation in prediction error estimation, IEEE Trans. Pattern Anal. Mach. Intell., 32,
634 569-575, <https://doi.org/10.1109/TPAMI.2009.187>, 2009.
- 635 Shi, X., Zhao, C., Jiang, J.H., Wang, C., Yang, X., and Yung, Y.L.: Spatial



636 representativeness of PM_{2.5} concentrations obtained using observations from network
637 stations, *J. Geophys. Res. Atmos.*, 123, 3145-3158,
638 <https://doi.org/10.1002/2017JD027913>, 2018.

639 Simmons, A.J., Untch, A., Jakob, C., Källberg, P., and Undén, P.: Stratospheric water
640 vapour and tropical tropopause temperatures in ECMWF analyses and multi-year
641 simulations, *Q J R Meteorol Soc.*, 125, 353-386,
642 <https://doi.org/10.1002/qj.49712555318>, 1999.

643 Van Donkelaar, A., Martin, R.V., and Park, R.J.: Estimating ground-level PM_{2.5} using
644 aerosol optical depth determined from satellite remote sensing, *J. Geophys. Res. Atmos.*,
645 111, D21201, <https://doi.org/10.1029/2005JD006996>, 2006.

646 Wang, Y., Yuan, Q., Li, T., Shen, H., Zheng, L., and Zhang, L.: Evaluation and
647 comparison of MODIS Collection 6.1 aerosol optical depth against AERONET over
648 regions in China with multifarious underlying surfaces, *Atmospheric Environ.*, 200,
649 280-301, <https://doi.org/10.1016/j.atmosenv.2018.12.023>, 2019.

650 Wu, X., Wang, Y., He, S., and Wu, Z.: PM_{2.5} / PM₁₀ ratio prediction based on a long
651 short-term memory neural network in Wuhan, China, *Geosci. Model Dev.*, 13, 1499–
652 1511, <https://doi.org/10.5194/gmd-13-1499-2020>, 2020.

653 Xu, P., Chen, Y., and Ye, X.: Haze, air pollution, and health in China, *Lancet*, 382,
654 2067, [https://doi.org/10.1016/S0140-6736\(13\)62693-8](https://doi.org/10.1016/S0140-6736(13)62693-8), 2013.

655 Yan, X., Zang, Z., Li, Z., Luo, N., Zuo, C., Jiang, Y., Li, D., Guo, Y., Zhao, W., Shi,
656 W., and Cribb, M.: A global land aerosol fine-mode fraction dataset (2001–2020)
657 retrieved from MODIS using hybrid physical and deep learning approaches, *Earth Syst.*
658 *Sci. Data*, 14, 1193-1213, <https://doi.org/10.5194/essd-14-1193-2022>, 2022.

659 Yan, X.: Physical and deep learning retrieved fine mode fraction (Phy-DL FMF),
660 Zenodo [data set], (Accessed on 30-09-2022), <https://doi.org/10.5281/zenodo.5105617>,
661 2021.

662 Yang, Q., Yuan, Q., Li, T., and Yue, L.: Mapping PM_{2.5} concentration at high
663 resolution using a cascade random forest based downscaling model: Evaluation and
664 application, *J. Clean. Prod.*, 277, 123887,



665 <https://doi.org/10.1016/j.jclepro.2020.123887>, 2020.

666 Yuan, Q., Shen, H., Li, T., Li, Z., Li, S., Jiang, Y., Xu, H., Tan, W., Yang, Q., Wang,
667 J., Gao, J., and Zhang, L.: Deep learning in environmental remote sensing:
668 Achievements and challenges, *Remote Sens Environ*, 241, 111716,
669 <https://doi.org/10.1016/j.rse.2020.111716>, 2020.

670 Zhang, Y., Li, Z., Bai, K., Wei, Y., Xie, Y., Zhang, Y., Ou, Y., Cohen, J., Zhang, Y.,
671 Peng, Z., Zhang, X., Chen, C., Hong, J., Xu, H., Guang, J., Lv, Y., Li, K., and Li, D.:
672 Satellite remote sensing of atmospheric particulate matter mass concentration:
673 Advances, challenges, and perspectives, *Fundamental Research*, 1, 240-258,
674 <https://doi.org/10.1016/j.fmre.2021.04.007>, 2021.

675 Zhang, Y., Li, Z., Chang, W., Zhang, Y., de Leeuw, G., and Schauer, J.J.: Satellite
676 observations of PM_{2.5} changes and driving factors based forecasting over China 2000–
677 2025, *Remote Sens.*, 12(16), 2518, <https://doi.org/10.3390/rs12162518>, 2020.

678 Zhang, Y., and Li, Z.: Remote sensing of atmospheric fine particulate matter (PM_{2.5})
679 mass concentration near the ground from satellite observation, *Remote Sens Environ*,
680 160, 252-262, <https://doi.org/10.1016/j.rse.2015.02.005>, 2015.